ARTICLE

A Scalable Fabrication Method for Gold Nanodisk-Upconverting Nanoparticle Hybrid Nanostructures

Received 00th January 20xx, Accepted 00th January 20xx

DOI: 10.1039/x0xx00000x

Taleb Ba Tisa, Cobi Sabob, Bo Xuc, Conrad Corbella Bagotb, Eric Rappeportb, Wounjhang Parka, b

Plasmonic nanostructures can be used to enhance the efficiency of upconversion nanoparticles (UCNPs) and enable new functionalities. However, the fabrication of these hybrid plasmon-UCNP nanostructures has traditionally relied on either wet-chemistry or nanolithography routes that are difficult to control, scale up, or both. In this work, we present a scalable nanofabrication process, capable of producing a massive array of gold-UCNP hybrid nanostructures over a few mm² area and with excellent uniformity in the photoluminescence intensity. This new approach combines the scalability of the bottom-up self-assembly method and the precision of the top-down nanolithography approach. It provides an efficient alternative route for the production of plasmonically enhanced UCNPs. A detailed discussion on the optimization of the UCNP self-assembly, the gold nanodisk lithography, and the nanopattern transfer processes is presented here. Additionally, we showcase the potential of this new approach for fabricating mechanical force sensors based on the selective plasmonic enhancement of the UCNP emission. This new approach holds a great potential in facilitating the production of plasmonically enhanced UCNPs that can be deployed for both imaging and sensing applications.

Introduction

Upconverting nanoparticles (UCNPs) have been at the center of many interesting applications in bioimaging^{1,2}, sensing^{3,4}, drug delivery^{5,6}, and optogenetics^{7,8}. They are typically composed of an inorganic host crystal such as NaYF₄ that is doped with rare-earth (RE) ions such as Yb3+, Er3+, and Tm³⁺. A key factor in the rising popularity and success of UCNPs is their ability to upconvert near infrared (NIR) excitation to visible light, thereby enabling bio-imaging and sensing with minimal noise from background autofluorescence. Moreover, UCNPs are largely unaffected by photobleaching or blinking9, making them ideal agents for long-term monitoring of live cells and tissues, which is often required in many biomedical applications^{10,11}. In addition, the rapid advances in the field of nanoparticle synthesis and surface modification offer an incredibly rich library of coatings, functional groups, and molecular labels that can be conjugated with UCNPs to enhance their chemical and physical properties and improve their biocompatibility^{12,13}.

Despite the many advantages offered by UCNPs, they suffer from a major flaw which is their poor efficiency compared to the conventional luminescent probes¹⁴. This low efficiency stems

upconversion, as well as the poor absorption of RE ions due to the forbidden nature of their 4f-4f optical transitions. Additionally, the presence of surface and lattice defects in the nanocrystals contributes to lower efficiency. To compensate for the poor optical performance, high excitation powers could be used, but doing so could severely limit the applicability of UCNPs in biological settings because of the increased possibility of cellular and tissue damage¹⁵. The ideal solution to this limitation is to enhance the UCNPs efficiency through either nanocrystal or photonic engineering¹⁶. With nanocrystal engineering, the enhancement arises from the suppression of the nonradiative energy pathways within the UCNPs. This can be done by optimizing the chemical composition or size of the nanocrystals^{17,18}, employing core-shell architectures^{19,20}, or using new host crystals that support efficient energy transfer processes between the RE ions^{21,22}. Photonic engineering, on the other hand, relies on increasing the local photonic density of states in the vicinity of UCNPs which in turn enhances their optical properties^{16,23}. This strategy is typically realized by coupling the UCNPs with an optical cavity whose resonance can be tuned to either the UCNPs excitation or emission bands. When the resonance targets the excitation wavelength, the cavity concentrates the electric field around the UCNPs, resulting in an effectively larger absorption cross-section and therefore stronger emission^{24–26}. The enhanced local field can also enhance the energy transfer between RE ions²⁷. When the resonance is tuned to the UCNP emission lines, it increases the spontaneous emission rates through the so-called Purcell effect28.

primarily from the requirement of multi-photon absorption for

Both absorption and Purcell enhancement of UCNPs have been demonstrated in the literature over the years. Many of

^a Materials Science and Engineering Program, University of Colorado. Boulder, CO 80303, U.S.A. * Corresponding email: won.park@colorado.edu

b. Department of Electrical, Computer and Energy Engineering, University of Colorado. Boulder, CO 80309-0425, U.S.A.

^c Department of Physics, University of Colorado. Boulder, CO 80309-0390, U.S.A.

[†] Footnotes relating to the title and/or authors should appear here.
Electronic Supplementary Information (ESI) available: [details of any supplementary information available should be included here]. See DOI: 10.1039/x0xx00000x

these demonstrations, however, employ large photonic crystals as their optical cavities 16,29,30 which inherently limit their compatibility with biomedical applications that call for nanoscale structures. The use of plasmonic nanocavities to enhance the UCNPs, on the other hand, provides an effective solution to this problem. Earlier attempts in this direction have focused on using chemical routes to synthesize plasmonic goldor silver-UCNP hybrid nanostructures^{31–34}. Despite their ability to produce nanoscale plasmonically enhanced UCNPs, these methods often rely on complex chemical reactions and lack precise control over the geometry. Alternatively, top-down nanolithography approaches have shown a promising potential in the production of plasmonically enhanced UCNPs with precise control over their physical dimensions and optical properties^{35,36}. However, these methods are slow, expensive, and usually difficult to scale up in comparison to the chemical routes.

In this paper, we report a scalable and efficient nanofabrication method to create gold-UCNP hybrid nanostructures with excellent uniformity over large areas. Our approach seamlessly integrates UCNP self-assembly with polymer thin film coating, laser interference lithography (LIL), nanopattern transfer, and dry and wet etching to produce a massive array of gold-UCNP hybrid nanostructures on glass substrates. We show that careful tuning of the self-assembly conditions results in the formation of densely packed monolayer films of UCNPs spanning a few mm² area with minimal aggregation and defects. We also show that the LIL conditions can be optimized to fabricate mm² -scale arrays of plasmonic gold nanodisks with diameters ranging from 100 to 230 nm. The ability to control the dimensions of the plasmonic nanodisks is important for tuning their plasmon resonance to overlap with the UCNP luminescent bands and achieve the desired upconversion enhancement.

To form the final hybrid structure, we further adapt a simple nanopattern transfer method, originally developed for 2D material transfer, to move the gold nanodisks from their native substrate onto the UCNP films. Our key contribution with regards to the transfer process is the utilization of an ultrathin layer of polydimethylsiloxane (PDMS) coating on top the UCNPs. This PDMS spacer layer not only facilitates the transfer of the gold nanodisks onto the UCNPs but also provides a straightforward way to modulate the upconversion enhancement. Following the transfer, we demonstrate that selective removal of excess PDMS and UCNPs can be achieved via dry and wet etching, using the gold nanodisks as etching masks. This final step leaves behind a large array of gold-UCNP hybrid nanostructures with high uniformity in geometry and photoluminescence emission. We conclude by presenting how the PDMS layer can be used to modulate the plasmonic enhancement of the UCNPs via mechanical pressing. This simple demonstration highlights the potential of this nanofabrication method to produce stimuli-responsive gold-UCNP hybrid nanostructures for biomedical imaging and sensing applications.

Experimental Section

Synthesis of NaYF₄: Yb, Tm upconversion nanoparticles

<u>Materials:</u> $YCl_3 \cdot 6H_2O$, $YbCl_3 \cdot 6H_2O$, $TmCl_3$, oleic acid (technical grade, 90%) (OA), 1-octadecene (technical grade, 90%) (ODE), and ammonium fluoride (NH₄F) were bought from Sigma-Aldrich. Solid sodium hydroxide (NaOH) pellets were purchased from Fisher Scientific.

Synthesis: 24.7%, 0.3 % Yb3+/Tm3+-doped UCNPs were synthesized via the thermal coprecipitation method. Briefly, 455 mg YCl₃·6H₂O, 191.4 mg YbCl₃·6H₂O, and 1.65 mg TmCl₃ were added to 36 mL ODE and 12 mL OA and heated under vacuum at 160°C for 30 minutes. A 20 mL methanol solution containing 200 mg NaOH and NH₄F was separately prepared. The ODE/OA solution was cooled down to 50°C, opened to atmosphere, and the methanol solution was added dropwise. This mixed solution was stirred for 30 minutes at 50°C, then heated to 100°C and put under vacuum for 20 minutes. The flask was then put under an argon atmosphere and heated to 300°C at a rate of 10°C/min. The solution was left at 300°C for 2 hours, cooled down naturally to less than 60°C, and transferred to two centrifuge tubes. Ethanol was added to the tubes to induce flocculation, and the UCNPs were collected by centrifugation (5400g, 10 minutes). The supernatant was removed, and the UCNPs were redispersed in hexane. Ethanol was added again, and the particles were centrifuged (5400g, 10 minutes). This redispersion process was repeated one more

The size and shape of the as-synthesized UCNPs were characterized using transmission electron microscopy (TEM) (Tecnai T12 Spirit 120kV Electron Microscope). The size distribution was calculated using the ImageJ software package.

Self-assembly of UCNP monolayer films

A stock solution of NaYF₄:Yb³⁺, Tm³⁺ nanocrystals was first prepared in CHCl₃ and allowed to settle overnight. In a 50 mL glass beaker, 30 µL (equivalent to 0.03 mg UCNPs) was drawn from the clear portion of the stock solution and added to 30 mL CHCl₃. Using a higher UCNPs concentration leads to the formation of multilayer and nonuniform films as discussed in the Results and Discussion. The solution was then sonicated for 30 seconds to ensure uniform UCNPs dispersion. DI water was gradually added to the beaker until it slightly overflowed, and then 200 µL of ethanol was carefully delivered just below the CHCl₃/water interface over a period of 5 to 10 seconds using a burette. The ethanol amount can be adjusted accordingly to reduce the number of bilayers/aggregates on the monolayer. After that, the burette was gently lifted, and the solution was allowed to stabilize for 10 minutes. The water layer was gradually removed until the surface tension of the CHCl₃ ruptured the water layer, creating a water ring around the beaker's edges. If needed, additional water droplets may be added to expand the water ring for easier scooping of the monolayer film. After the ring formation, the beaker was covered with a watch glass and left to stabilize for another 15 minutes. Finally, a 1.5x1.5 cm² coverslip was gently inserted at the edge of the water ring and lifted at an angle to collect the

UCNP monolayer film from the water/air interface. The coverslips containing the UCNPs were cleaved into $^{\sim}$ 0.5x0.5 cm² substrates, which were then sonicated in CHCl₃ for 30 seconds to remove any large UCNPs aggregates or glass shards resulting from the cleaving step.

Ultrathin PDMS thin film fabrication

A commercially available silicon elastomer kit (SYLGARD 184, Dow Corning, USA) was used to fabricate the ultrathin PDMS film coating on the UCNPs monolayer. Briefly, a 1:10 (w/w) ratio of the prepolymer base and curing agent were thoroughly mixed for 5 minutes in a clean weighing boat. The boat was then placed under vacuum until all air bubbles created during mixing were removed. Subsequently, a 1 wt% stock solution of the PDMS mixture was prepared in hexane, vortexed for 5 minutes, and left to nutate overnight. Following this, few droplets of the PDMS stock solution were added onto the UCNP monolayer substrates, and spin-coated for 30 seconds at 5000 RPM under maximum acceleration. Finally, the PDMS-coated substrates were cured on a hotplate at 55 °C for 24 hours.

Fabrication of gold nanodisks

A negative photoresist (NR9-1000PY, Futurrex) was first spun on a silicon wafer for 5 seconds at 500 RPM followed by 40 seconds at 8000 RPM. The thickness of the photoresist (PR) film was normally around 600 nm. To reduce the PR layer thickness to 160 nm, a 1:1 (v/v) dilution of NR9-1000PY with cyclohexanone was used while the spin-coating conditions were kept unchanged. The wafer was then baked at 150 °C for 1 minute and cleaved into ~ 1x1 cm² small substrates for the lithography step. The pre-baking temperature can be reduced to 125 °C to enable the fabrication of small gold nanodisks with decent yield.

A home-built Llyod's mirror laser interference lithography (LIL) setup with a 325 nm HeCd laser (Kimmon) was used for patterning the PR layers. The laser output power was reduced using a ND filter and the exposure dose was adjusted by controlling the sample exposure time. The LIL period was adjusted via a rotating stage that controls the angle at which the Lloyd mirror and the PR substrate are exposed to the laser beam. To create a nanohole array pattern, the exposure was repeated twice, with the PR substrate rotated 90 degrees the second time. After this, the substrates were baked at 100 °C for 1 minute before they were immersed in the developer solution (RD-6, Futurrex) for 15 seconds. Following the lithography, a 30 nm thick gold layer was thermally evaporated onto the substrates to create the gold nanodisks. Finally, the remaining resist was lifted off by soaking the substrates in acetone and sonicating for 5-10 seconds.

Gold nanodisk transfer

A 4% solution of polymethylmethacrylate (PMMA) in anisole was spun onto the gold nanodisks substrates, followed by baking at 185 °C for 5 minutes. After cooling down to room temperature, the edges of the PMMA films were carefully scratched off (~ 0.5 mm from each side) using a razor blade to

expose the Si surfaces to the etchant in the next step. Subsequently, the PMMA-coated substrates were gently placed on top of the 3% (w/w) NaOH etching solution. The temperature of the etching solution was kept elevated using a hot water bath. Once the PMMA film containing the gold nanodisk array separates from the carrier Si substrates, a microscope slide was used to scoop it and transfer it to a clean DI water bath. At this point, the PDMS-coated substrates were treated with O_2 plasma (30s, 50 W, and 8 sccm) to improve their adhesion with the gold nanodisk. The PMMA film was then transferred onto the treated-PDMS substrate and baked at 80 °C for 5 minutes. Finally, the PMMA carrier film was removed from the PDMS-substrate by soaking in a hot acetone bath for another 5 minutes, followed by acetone and water rinse.

RIE and HCl etching

The reactive ion etching chamber was first conditioned by performing O_2 ashing (200 sccm, 500 W) for 10 minutes, followed by a 30s purging with the PDMS etching recipe. This step helped stabilize the plasma during the actual etching stage. The PDMS etching recipe consisted of a 15:5 (sccm: sccm) mixture of Ar:CF₄, operating an RF power at 200 W and a base pressure of 30 millitorr. When the preconditioning was completed, the sensor substrates were placed inside the RIE chamber, and the etching recipe was run again for a total of 120 seconds. Following the PDMS etching process, the background UCNPs were etched away by immersing the substrates in a magnetically stirred hydrochloric acid (HCl) solution (pH $^{\sim}$ 1.3) for 30 seconds, after which they were rinsed with water.

To determine the PDMS etching rate, we tested the etching recipe with PDMS film that was coated with a negative PR layer. The PR layer was patterned with LIL to create a grating profile with periodically exposed and protected PDMS regions. When we ran the etching recipe on this sample, the exposed PDMS regions were attacked by etchant CF_4 gas whereas the regions protected by the PR remained intact. Upon the PR removal using acetone, a periodic PDMS grating was obtained across the entire PDMS film. The height of the grating steps as a function of etching time was then used to calculate a PDMS etching rate of ~ 0.6 nm/s.

Results and Discussion

Our nanofabrication strategy is shown schematically in Fig. 1. It consists of three stages, dedicated to the fabrication of the various components (i.e., UCNP monolayer, PDMS film, and gold nanodisks) and their integration into the final hybrid nanostructure. In the first stage, a self-assembled monolayer of UCNPs is prepared on a glass substrate, followed by spincoating of an ultrathin PDMS layer. In the second stage, gold nanodisks are fabricated on a separate silicon (Si) substrate using LIL, followed by lift-off. And in the third and final stage, the gold nanodisks are transferred from their native substrate onto the PDMS-coated UCNP monolayer via a polymer-assisted nanopattern transfer method. Dry and wet etching are then used to remove excess PDMS and UCNPs from the background

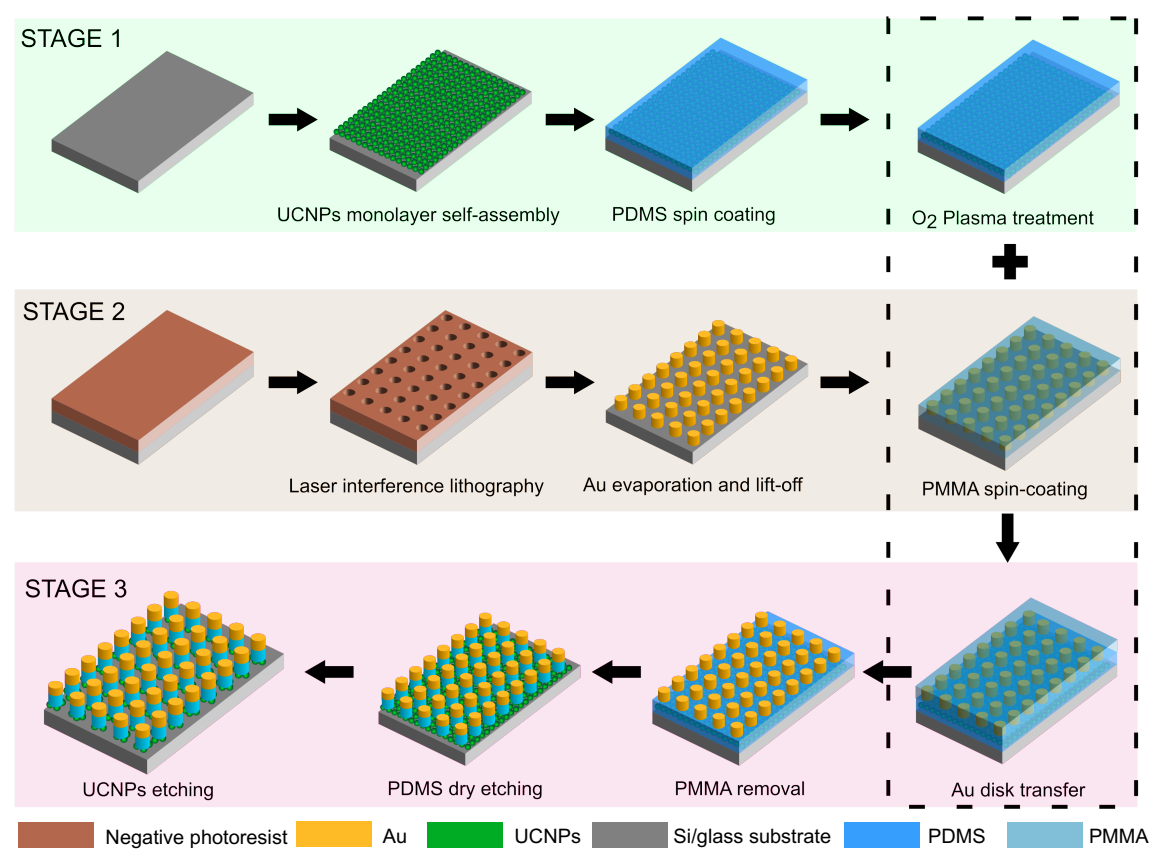


Figure 1. A schematic showing the overall flow of the nanofabrication method.

of the hybrid nanostructures, respectively. With the completion of the last step, a large array of gold-UCNP hybrid nanostructures is obtained, covering a mm²-scale area.

Stage 1: UCNP Monolayer and Ultrathin PDMS Films Fabrication

The first stage begins with the synthesis of NaYF₄: Yb³⁺, Tm³⁺ UCNPs using the well-established thermal coprecipitation method^{4,37,38}. The as-synthesized UCNPs exhibited a narrow size distribution, with an average diameter of 32.6 nm and a standard deviation of only 1.6 nm (Fig. S1). The uniformity in shape and size plays a critical role in the self-assembly process of UCNPs as shown in previous reports^{39,40}. Following the synthesis, the UCNPs were dispersed in chloroform to make a stock solution with a concentration of 10 mg/mL, which was allowed to settle overnight before further use. The selfassembly process, shown schematically in Fig. 2(A), has been successfully used to create densely packed monolayer films of UCNPs⁴¹. Fundamentally, it relies on the reduction of the interfacial energy between two immiscible liquids, specifically water and chloroform, by entrapping the nanoparticles at the interface where the two liquids meet^{41,42}. The process starts with the agitation of the UCNPs in the chloroform phase via the addition of ethanol, as shown in step 2 of Fig. 2(A). Ethanol's miscibility with both chloroform and water disrupts the surface tension between them, allowing the UCNPs to start populating the interfacial region. However, owing to their hydrophobic nature, the UCNPs tend to minimize their interaction with the aqueous phase by forming a densely packed film at the interface. The presence of this film, acting as a barrier between chloroform and water, reduces the overall interfacial energy of the system and is thus thermodynamically more favorable than the dispersion of UCNPs back into the chloroform phase. The thickness and uniformity of the resulting UCNP film is dependent on the extent of the UCNP agitation, a process controlled by the initial UCNPs concentration in the chloroform phase and the volume of ethanol introduced. Once the desired UCNP film is successfully formed, excess water is removed, and the film is carefully collected using a glass coverslip, as shown in step 3 of Fig. 2(A).

To obtain a densely packed UCNP monolayer film, we control the UCNP agitation by carefully adjusting the UCNP concentration and the ethanol volume. At a concentration of 0.33 mg/mL and ethanol volume of 800 μL, we observe that only thick and highly non-uniform multilayered UCNP films formed, Fig. 2(B). The formation of these films indicates that our UCNPs have a low threshold for agitation and thus a lower UCNP concentration should be used for the monolayer formation. Indeed, lowering the UCNP concentration to 0.01 mg/mL results in mostly monolayer films, Fig. 2(C). The quality of these monolayer films is further improved by reducing the ethanol volume from 800 to 200 μL, as shown in Fig. 2(D) and Fig. S2(A-B). Introducing smaller volumes of ethanol slows down the agitation process, and consequently minimizes the tendency of UCNPs to aggregate or form bilayer regions. The self-assembled UCNP monolayer spans an area of a few mm² with good uniformity and coverage as shown in Fig. 2(E).

In the next step, the cleaned UCNP monolayers are coated with an ultrathin PDMS layer. The PDMS is prepared from the commercial SYLGARD 184 kit by thoroughly mixing the prepolymer base with the curing agent at a ratio of 10 to 1. This mixture is then diluted in hexane to prepare stock solutions for the spin-coating process. The concentration of the stock solutions determines the thickness of the PDMS thin film⁴³. As shown in Fig. S3, increasing the PDMS concentration leads to thicker PDMS film and thus taller nanostructures. Because the thickness of the gold is well-controlled across the substrate during the thermal evaporation process, the variation in the height of the nanostructures is attributed mostly to the variation in the spin-coated PDMS layer thickness. Following the spin-coating process, the substrates are baked at 55 °C overnight to fully cure the PDMS on the UCNPs before the next stage. With the PDMS coating done, the first stage of the nanofabrication method is completed.

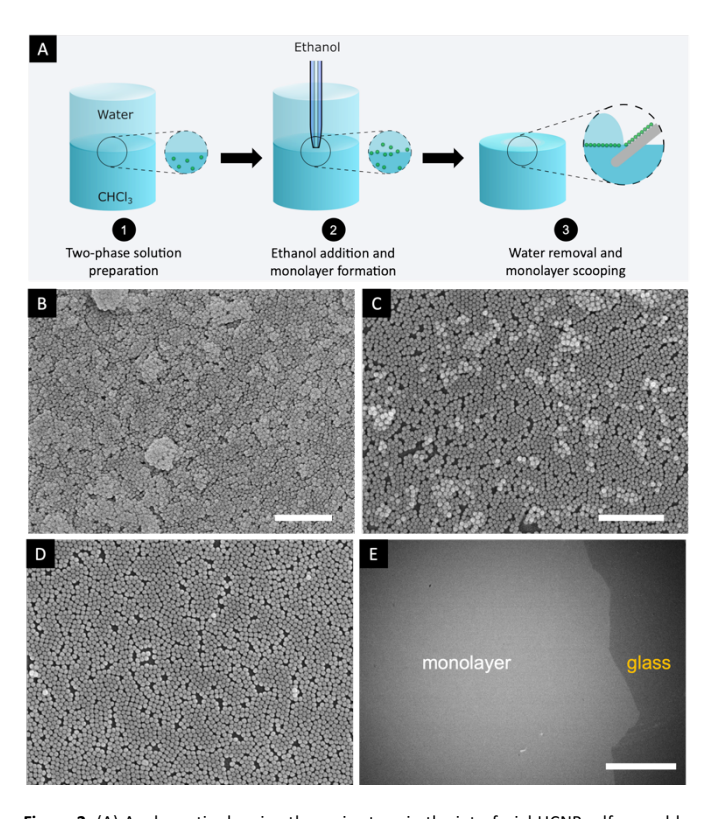


Figure 2. (A) A schematic showing the main steps in the interfacial UCNP self-assembly process. SEM images of (B) multilayered UCNP film (UCNPs: 0.33 mg/mL, ethanol: 800 μL), (C) mostly single-layered UCNP film (UCNPs: 0.01 mg/mL, ethanol: 800 μL), (D) close-packed UCNP monolayer film (UCNPs: 0.01 mg/mL, ethanol: 200 μL). Scale bar is 500 nm. (E) Low magnification SEM image showing the large-scale coverage of the UCNPs monolayer film. Scale bar is 500 μm.

Stage 2: Gold Nanodisk Fabrication

In the second stage of the process, the gold nanodisks are fabricated using LIL. The cost-effectiveness and speed of this technique render it an attractive option for scalable nanofabrication compared to other, more complex, costly, and time-consuming methods such as electron beam lithography⁴⁴. Moreover, LIL provides a simple way to control the diameters of the gold nanodisks. This is typically done by adjusting the angle

of the Lloyd's mirror with respect to the incident laser beam which in turn changes the period of interference fringes. Shorter periods lead to smaller diameters in general. By adjusting the diameter of the gold nanodisks, their plasmon resonance can be tuned to match the luminescence bands of the UCNPs.

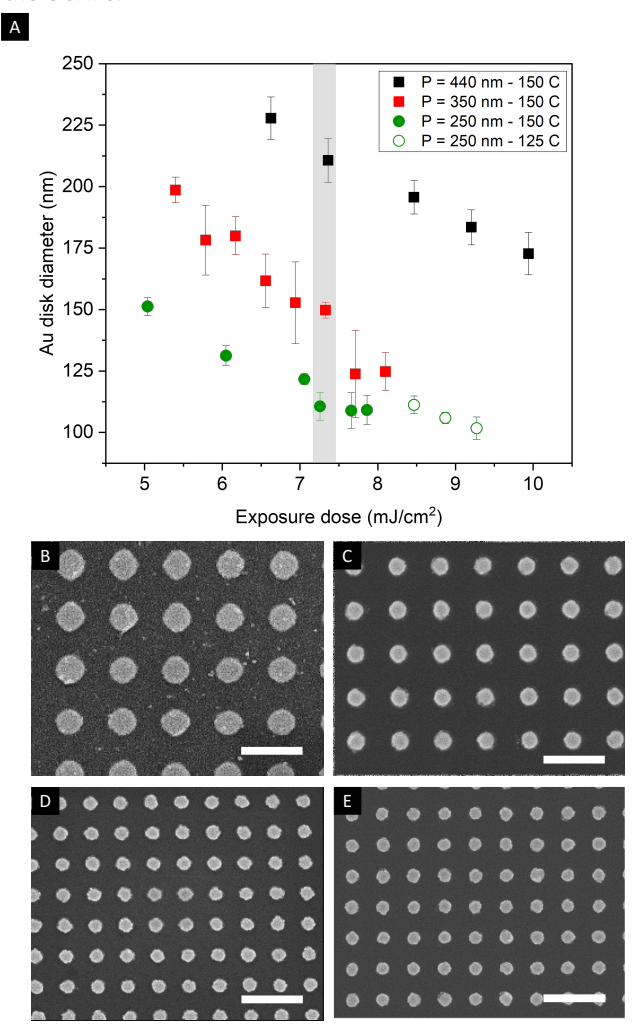


Figure 3. (A) Diameters of the fabricated gold nanodisks as a function of the exposure dose and LIL period P. Squares (■) and circles (●) refer to photoresist thicknesses of 600 and 160 nm, respectively, while the temperature refers to the pre-baking condition used. (B-D) SEM images of gold nanodisks fabricated with an exposure dose of 7.3 mJ/cm² (greyed out region in (A)), prebaking temperature of 150°C, and P = 440, 350, and 250 nm, respectively. (E) SEM of gold nanodisks fabricated with an exposure dose of 9.3 mJ/cm², prebaking temperature of 125 °C, and P = 250 nm. Scale bar is 500 nm.

After the PR spin-coating and pre-baking step, the substrates are exposed to the laser light twice, with a 90-degree rotation in between the two exposures, followed by post-baking and development to create a nanohole array pattern (Fig. S4(A-C)). The gold nanodisks are subsequently fabricated by depositing a 30 nm thick layer of gold using thermal evaporation. Due to the directionality of the gold evaporation process, the diameter of the gold nanodisks closely matches that of the nanoholes as shown in Fig. S4(D-G). The sideview profile in Fig. S4(G) confirms that the thickness of the gold nanodisks is ~ 30 nm as expected. Finally, the PR template is

lifted off using a combination of acetone soaking and brief sonication, leaving behind a large array of gold nanodisks.

As shown in Fig. 3(A), the diameter of the gold nanodisks is adjusted by tuning the interference period and exposure dose, which is defined as the total light energy per area. With a period of 440 nm, we can tune the diameters from 225 to 175 nm by increasing the LIL exposure dose. Reducing the period down to 350 nm allows us to expand the range of diameters to 125 nm using similar exposure doses. Further reduction of the period to 250 nm, however, is more challenging because, with higher exposure time, only shallow indentations on the PR will form rather than holes. This is likely caused by a slower development rate due to the high aspect ratio of the small nanoholes which limits the diffusion of the PR materials out of the nanoholes during the development process. To mitigate this issue, we first reduce the thickness of the PR layer from 600 to 160 nm by diluting the PR with cyclohexanone at a ratio of 1:1 (v/v). As shown in Fig. 3(A), this thickness reduction allows us to expand the range of gold nanodisks diameters to 110 nm. To push the range even further, we modified the PR pre-baking temperature from 150 to 125 °C. Lower pre-baking temperatures result in less dense PR films that retain more of their solvent and thus tend to have higher development and diffusion rates⁴⁵. As shown in Fig. 3(E) and Fig. S5(B-C), this simple modification allows us to fabricate gold nanodisks as small as 100 nm quite reliably and over a large area. Fig. 3(B-D) show representative gold nanodisks fabricated at roughly the same exposure dose and with a period of 440, 350, and 250 nm, respectively.

Stage 3: Nanopattern Transfer and Etching

In the final stage of this nanofabrication method, the components from the previous stages are combined into an array of gold-UCNP hybrid nanostructures. To achieve this, we adapted a nanopattern transfer protocol originally developed for MoS₂ to move the gold nanodisks from their native Si substrate onto the PDMS-coated UCNP substrate⁴⁶. A schematic of the transfer process is presented in Fig. 4(A). The process uses a dissolvable polymer film as an intermediate carrier between the source and target substrates. Following the coating of the source substrate with the carrier polymer, the source substrate is etched in a basic solution, allowing the polymer carrier to separate from it (Fig. 4(A), step 1-2). When the polymer carrier is completely separated, it is moved to a water bath where it can be transferred onto the target substrate (Fig. 4(A), step 3). Once the transfer is done, the polymer carrier is dissolved in a suitable solvent, leaving behind the nanostructures it carried from the source substrate.

We use polymethylmethacrylate (PMMA) as our polymer carrier during the transfer process. As shown in Fig. 4(B), we spin-coat a PMMA thin film on top of the Si substrate carrying the gold nanodisks. The PMMA is then baked at 185 °C, well above its glass transition temperature, to soften and wrap more effectively around the gold nanodisks. After cooling to room temperature, the edges of the PMMA film are scratched off to provide the etchant a direct access to the topmost surface of the Si substrate. The etching of Si was done using a warm 3%

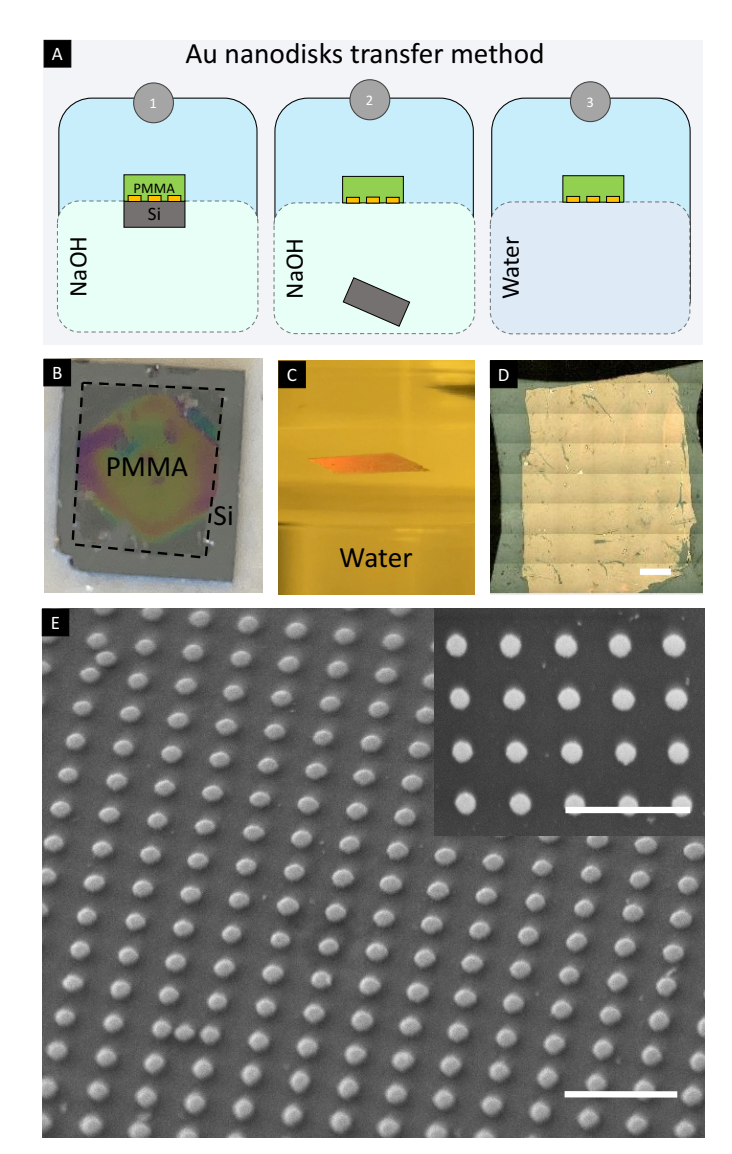


Figure 4. (A) Schematic showing the nanoarray transfer method. In step 1, the PMMA-coated Si substrate is placed on a warm 3wt% NaOH solution. In step 2, the basic solution etches the carrier Si substrate, allowing the PMMA with the plasmonic nanoarray to separate from it. In step 3, the PMMA film is moved to a separate water bath where it is transferred onto the PDMS-coated UCNPs. (B) Picture showing the Si substrate carrying the gold nanodisk array after the PMMA coating. (C) Picture of the PMMA film carrying the gold nanodisk array after it separated from the Si substrate and moved to a water bath. The interference from the PMMA film indicates a decent transfer of the gold nanodisk array. (D) Micrograph of the gold nanodisk array after being transferred on the PDMS-coated UCNPs and soaked in hot acetone to dissolve the PMMA carrier film. Scale bar is 1 mm. (E) SEM image of the transferred gold nanodisk array on PDMS showing decent coverage. Inset shows that the periodicity and shape of the gold nanodisks are preserved during the transfer. Scale bar is 1 μm.

(w/w) NaOH solution. After 20 to 30 minutes, the PMMA film is fully separated from the Si substrate, carrying with it all the gold nanodisks. As shown in Fig. 4(C), the PMMA film shows a bright red color, caused by the periodicity of the gold nanodisks array. This structural color can be seen across the entire PMMA film, indicating a high transfer yield, as well as good uniformity. To enable an efficient transfer of the PMMA film, we first treat the PDMS-coated substrate with O_2 plasma. This light plasma treatment plays two crucial roles. First, it renders the PDMS film more hydrophilic⁴⁷ so that water can wet it more effectively and

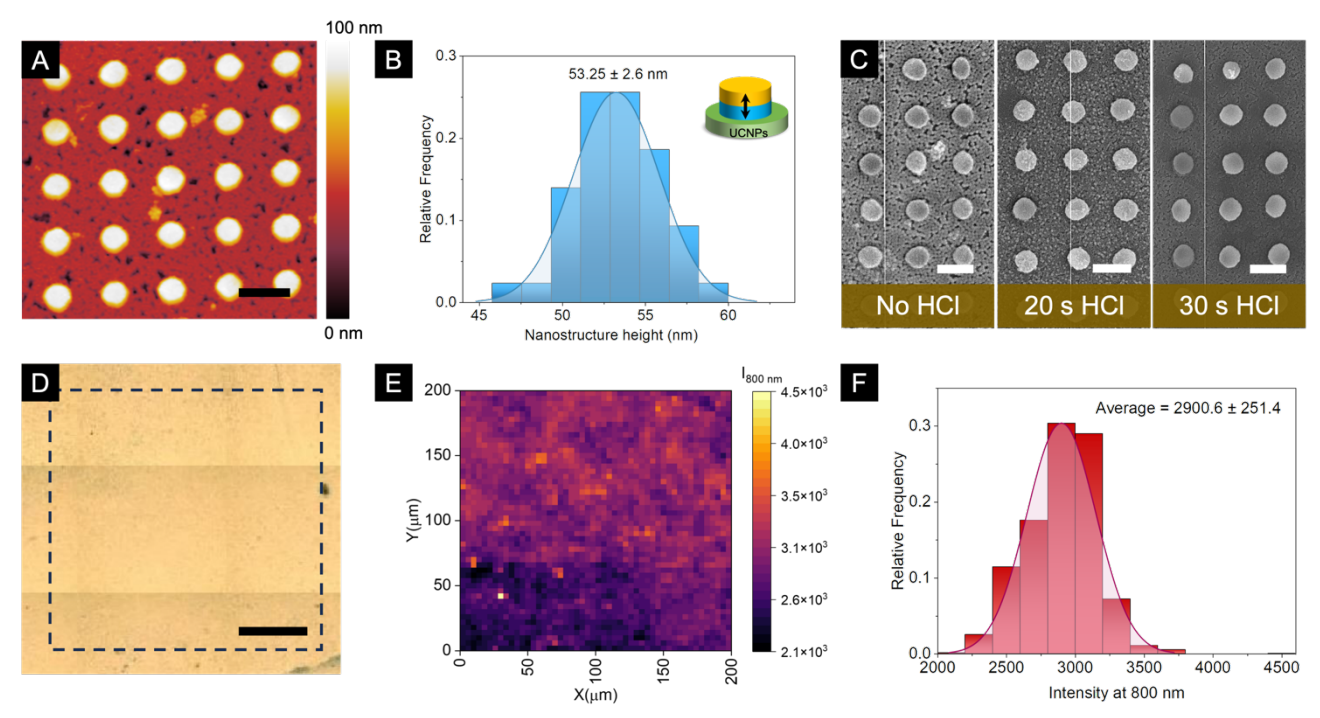


Figure 5. (A) AFM map of the gold-UCNP hybrid nanostructures after the PDMS dry etching. It shows that the UCNPs in background get exposed after PDMS etching. Scale bar is 400 nm. (B) Hybrid nanostructure height distribution before UCNP etching as calculated from a 3x3 um² AFM map. The height corresponds to the sum of the gold nanodisk thickness which is 30 nm and the PDMS thin layer. (C) SEM images showing the extent of HCl etching at various time intervals. Scale bar is 350 nm. (D) Micrograph of the gold-UCNP hybrid nanostructure after the HCl etching. Scale bar is 50 μm. (E-F) PL map and intensity histogram showing the distribution of the 800 nm intensity collected from the gold-UCNP hybrid across an area of 200x200 μm².

the floating PMMA film can easily be scooped with minimal wrinkling and folding. Secondly, O2 treatment has been shown to enhance the adhesion of PDMS with other materials⁴⁸ and hence can be used to improve the fidelity of the gold nanodisks transfer onto PDMS. After the PMMA film is successfully transferred, the substrate is baked at 80 °C to evaporate any water residue and allow better contact between the gold nanodisks and the PDMS film. Following this step, the PMMA is washed off by soaking the substrate in a hot acetone bath, leaving behind a large array of gold nanodisks on PDMS-coated UCNPs. The transferred area, as seen in Fig. 4(D), spans roughly 5×7 mm² and shows minimal defects throughout that area. With a period of 350 nm, this area contains hundreds of millions of gold nanodisks. Fig. 4(E) shows that the periodicity and quality of the gold nanodisks is preserved during the transfer process.

The next step in this stage is to remove the excess PDMS using reactive ion etching (RIE). During this step, the transferred gold nanodisks function as physical masks, enabling the selective etching of PDMS between the nanostructures. This recipe yields a moderate PDMS etching rate of 0.6 nm/s (Fig. S6), thus minimizing the physical damage that the gold nanodisks sustain during the etching process. As shown in Fig. 5(A, C), the successful removal of the PDMS is evidenced by the exposure of the UCNPs in the background of the hybrid nanostructures. This is in contrast to Fig. 4(E) where the PDMS is completely covering the UCNPs prior to the RIE step. The PDMS under the gold nanodisks is protected during etching, as confirmed by the height of the nanostructures, Fig. 5(B) which

is equal to the gold nanodisk thickness plus the PDMS layer thickness. Considering that the deposited gold thickness is 30 nm, the PDMS layer under the nanodisks is around 23 nm in thickness. The small variation in the overall height (< 5%) across a 3x3 µm² area reflects the excellent uniformity of the initial gold and PDMS thin films used in the construction of the hybrid nanostructures. After the PDMS etching, the exposed UCNPs in the background are etched away by soaking the substrates in an HCl solution with pH of ~ 1.3. By increasing the HCl etching time from 20 to 30 seconds, the exposed UCNPs are completely removed, leaving behind only gold-UCNP nanostructures on the substrate as shown in Fig. 5(C). To confirm that the UCNPs in the hybrid nanostructure are still intact after the HCl etching, we took a photoluminescence (PL) map over an area of 200 × 200 μm² under 980 nm excitation (Fig. 5(D-E)). As shown in Fig. 5 (F), the variation in the 800 nm luminescence intensity of the hybrid nanostructures across this area is less than 9%, confirming both the presence of the UCNPs and their excellent uniformity.

Potential Application: Mechanical Force Sensing

One potential application of the hybrid nanostructure is mechanical force sensing. In this application, the elasticity of the PDMS layer separating the gold nanodisks and UCNPs is exploited to modulate the Purcell enhancement as the nanostructure is subjected to an external mechanical force. A compressive force would effectively reduce the PDMS thickness. As the separation between the gold nanodisks and UCNPs is reduced, the Purcell effect is expected to become stronger, increasing the luminescence intensity, provided that

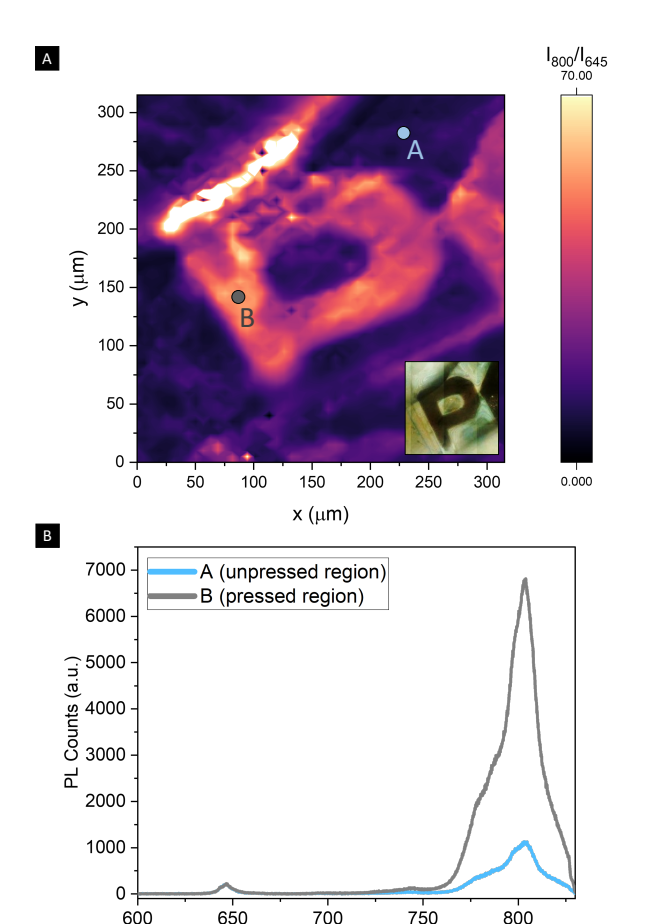


Figure 6. (A) PL map showing the ratio between the 800 and 645 nm emission lines of gold-UCNP hybrid nanostructures under mechanical pressing using a "P" letter shaped stamped. The region above the P letter shows very high ratios because of a fracture in the sensor substrate during the pressing which resulted in very low counts. The inset is a bright field micrograph of the "P" stamp being pressed on the substrate carrying the hybrid nanostructures. (B) PL spectra of two regions representing unpressed (A) and pressed hybrid nanostructures, as shown in Fig. 6(A)

Wavelength (nm)

quenching does not dominate³³. This allows for the determination of external force from the measured luminescence intensity. To demonstrate this feature, we first fabricate a hybrid nanostructure whose plasmon resonance is tuned to overlap the 800 nm luminescence of UCNP. Further, we fabricate a letter "P" on a glass substrate using the standard photolithography and employ it as a stamp to press on the gold-UCNP hybrid nanostructures, as shown in the inset of Fig. 6(A). As evidenced by the higher PL intensity ratio in Fig. 6(A), the 800 nm emission of the hybrid nanostructures residing under the letter "P" is enhanced more strongly by the gold nanodisks due to the effectively thinner PDMS spacer layer. Here, we use 800nm/645nm intensity ratio as the signal, rather than the 800 nm intensity itself, in order to take advantage of the additional benefits of ratiometric sensing³³.

By comparing the PL spectra taken from two points in unpressed and pressed regions (Fig. 6(B)), we can indeed see a significant increase in the 800 nm emission in the pressed region. The variations in the PL ratio of the pressed region are likely caused by surface roughness of the stamp and nonuniformity of the pressing. Nevertheless, this simple

method of modulating the UCNP emission can in principle be utilized to fabricate mechanical force or tactile sensors based on gold-UCNP hybrid nanostructures. A detailed study on the optical properties of the hybrid nanostructures under external force is to be presented in a separate paper. Additionally, it is noted that the hybrid gold-UCNP nanostructures can be used for a variety of other types of sensing by replacing the PDMS spacer layer with a different material that is responsive to other types of stimuli such as temperature, humidity, or the pH level, to mention a few examples.

Conclusions

In this work, we present a scalable and efficient nanofabrication method to create a large array of gold-UCNP hybrid nanostructures over a mm²-scale area. By combining the bottom-up nanoparticle self-assembly with top-down lithography using a nanopattern transfer process, the new fabrication method can produce heterogeneous nanostructures exactly in the prescribed geometry. It allows us to use high quality luminescent nanoparticles which are usually synthesized by wet-chemistry methods and combine them with lithographically fabricated plasmonic nanostructures precisely tuned for the desired geometry and resonance wavelengths. It is thus possible to accurately control the plasmonic interaction and the resulting optical properties. Furthermore, using a scalable lithography technique like LIL, it can produce a massive array of hybrid nanostructures, making it applicable to a wide range of bioimaging and sensing applications.

To improve the scalability and efficiency of the fabrication process, we first investigated the roles that the UCNPs concentration and ethanol volume have on the quality of the self-assembly monolayer films. We showed that by adjusting both parameters, it is possible to fabricate densely packed selfassembled UCNP monolayer films over mm²-areas. Having these high quality UCNP films enable the spin-coating of ultrathin PDMS films with uniform thicknesses (< 5% variation). Additionally, we systematically studied the factors impacting the fabrication of gold nanodisks using LIL. We showed that by controlling the exposure dose, photoresist thickness, prebaking temperature, gold nanodisks with diameters ranging from 100 to 230 nm can be reliably made over mm²-scale areas. We also showed a high-fidelity transfer of the gold nanodisks from their native Si substrates onto the PDMS-coated UCNPs using a simple polymer-assisted transfer method coupled with a light O₂ plasma treatment of the PDMS layer.

In the last step of the fabrication process, we demonstrated that the gold disks can in fact be used as etching masks, thereby enabling the selective removal of excess PDMS and UCNPs from the underlying layers. This final etching step results in the creation of a large array of gold-UCNP hybrid nanostructures spanning a few mm². The quality of the array was confirmed via PL intensity map, which revealed a uniform optical behavior (< 9% variation) over a $200\times200~\mu\text{m}^2$ area. Finally, thanks to the elastic behavior of PDMS spacer layer, we were able to showcase a promising use of the fabricated hybrid nanostructures in sensing mechanical forces. Potentially, other

types of sensors could be made by simply replacing the PDMS with other stimuli-responsive materials.

Author Contributions

Conceptualization, funding acquisition, methodology, project administration, supervision: WP; Investigation, data curation, visualization: TBT, CS, BX, CCB, ER; Writing – original draft: TBT; Writing – review & editing: TBT, BX, CCB, WP.

Conflicts of interest

W. P. has a stake in Irradiation Sensing Corp. The remaining authors have no competing interests to declare.

Acknowledgements

The work is supported in part by the National Science Foundation (CBET 2029559), National Institute of Health (R21 GM140347), Department of Education (GAANN P200A180012, P200A210111) and Colorado Office of Economic Development and International Trade (DO 2023-2330).

Notes and references

- 1 E. M. Mettenbrink, W. Yang and S. Wilhelm, *Adv Photonics Res*, 2022, **3**, 2200098.
- 2 W. Lv, J. Ye, Q. Wang, C. Li, J. Wang, Z. Zhang, N. Niu, Z. Liu, J. Xu and Y. Fu, *ACS Appl Nano Mater*, 2022, **5**, 9367–9378.
- 3 M. Meng, T. Zhang, J. Wang, Z. Cheng, Z. Li, X. Qiao, J. Wen, U. R. Genger, W. Long and J. Ou, *Opt Mater (Amst)*, 2023, **136**, 113389.
- 4 C. Corbella Bagot, E. Rappeport, A. Das, B. Tis, W. Park, C. C. Bagot, E. Rappeport, W. Park, A. Das and T. B. Tis, *Adv Opt Mater*, 2022, **10**, 2200242.
- 5 Q. Liu, H. B. Cheng, R. Ma, M. Yu, Y. Huang, L. Li and J. Zhao, *Nano Today*, 2023, **48**, 101747.
- 6 J. H. Yan, K. Shao, L. J. Wu, J. Hu, M. M. Man, X. Q. Li, X. Y. Kong and J. S. Shi, *ACS Appl Nano Mater*, 2022, **5**, 15473–15487.
- 7 J. Yan, Y. Wan, Z. Ji, C. Li, C. Tao, Y. Tang, Y. Zhang, Y. Liu, J. Liu, J. Yan, C. Li, C. Tao, J. Liu, Y. Wan, Z. Ji, Y. Tang, Y. Zhang and Y. Liu, *Adv Funct Mater*, 2023, 2303992.
- 8 D. Maemura, T. S. Le, M. Takahashi, K. Matsumura and S. Maenosono, *ACS Appl Mater Interfaces*, 2023, **15**, 42196–42208.
- 9 S. Wu, G. Han, D. J. Milliron, S. Aloni, V. Altoe, D. V. Talapin, B. E. Cohen and P. J. Schuck, *Proc Natl Acad Sci U S A*, 2009, **106**, 10917–10921.
- 10 X. Wang, J. Fu, C. Jiang, X. Liao, Y. Chen, T. Jia, G. Chen, X. Feng, X. Wang, X. Feng, C. Jiang, T. Jia, G. Chen, J. Fu, X. Liao and Y. Chen, *Advanced Materials*, 2023, **35**, 2210948.
- 11 Y. Da, S. Luo and Y. Tian, *ACS Appl Mater Interfaces*, 2022, **15**, 138–157.

- 12 E. Andresen, F. Islam, C. Prinz, P. Gehrmann, K. Licha, J. Roik, S. Recknagel and U. Resch-Genger, *Scientific Reports 2023 13:1*, 2023, **13**, 1–13.
- 13 H. Zhang, X. Wang, R. Jin and Q. Su, Giant, 2022, 12, 100130.
- 14 X. Li, F. Zhang and D. Zhao, Nano Today, 2013, 8, 643-676.
- 15 Q. Liu, Y. Zhang, C. S. Peng, T. Yang, L. M. Joubert and S. Chu, *Nature Photonics 2018 12:9*, 2018, **12**, 548–553.
- 16 A. Das, K. Bae and W. Park, Nanophotonics, 2020, 9, 1359–1371.
- 17 S. Wen, D. Li, Y. Liu, C. Chen, F. Wang, J. Zhou, G. Bao, L. Zhang and D. Jin, *Journal of Physical Chemistry Letters*, 2022, **13**, 5316–5323.
- 18 C. Ma, C. Shan, K. Park, A. T. Mok, P. J. Antonick and X. Yang, *Nanophotonics*, 2020, **9**, 1993–2000.
- 19 Y. Zhang, R. Wen, J. Hu, D. Guan, X. Qiu, Y. Zhang, D. S. Kohane and Q. Liu, *Nature Communications* 2022 13:1, 2022, **13**, 1–12.
- 20 P. Ren, X. Zheng, J. Zhang, S. De Camillis, J. Jia, H. Wang, X. Liao, J. A. Piper and Y. Lu, *ACS Photonics*, 2022, **9**, 758–764.
- 21 J. Wang, R. Deng, M. A. Macdonald, B. Chen, J. Yuan, F. Wang, D. Chi, T. S. Andy Hor, P. Zhang, G. Liu, Y. Han and X. Liu, *Nature Materials* 2013 13:2, 2013, **13**, 157–162.
- 22 S. Nacak and M. U. Kumke, *The Journal of Physical Chemistry C*, 2023, **39**, 19629-19642.
- 23 W. Park, D. Lu and S. Ahn, 2940 / Chem. Soc. Rev, 2015, 44, 2940.
- 24 D. Lu, S. K. Cho, S. Ahn, L. Brun, C. J. Summers and W. Park, *ACS Nano*, 2014, **8**, 7780–7792.
- 25 A. Das, C. Mao, S. Cho, K. Kim and W. Park, *Nat Commun*, 2018, **9**, 1–11.
- 26 C. Mao, K. Min, K. Bae, S. Cho, T. Xu, H. Jeon and W. Park, *ACS Photonics*, 2019, **6**, 1882–1888.
- 27 D. Lu, C. Mao, S. K. Cho, S. Ahn and W. Park, *Scientific Reports* 2016 6:1, 2016, **6**, 1–11.
- 28 P. Anger, P. Bharadwaj and L. Novotny, *Phys Rev Lett*, 2006, **96**, 113002.
- 29 C. Würth, P. Manley, R. Voigt, D. Ahiboz, C. Becker and U. Resch-Genger, *Nano Lett*, 2020, **20**, 6682–6689.
- 30 C. Gong, W. Liu, N. He, H. Dong, Y. Jin and S. He, *Nanoscale*, 2019, **11**, 1856–1862.
- 31 D. Mendez-Gonzalez, S. Melle, O. G. Calderón, M. Laurenti, E. Cabrera-Granado, A. Egatz-Gómez, E. López-Cabarcos, J. Rubio-Retama and E. Díaz, *Nanoscale*, 2019, **11**, 13832–13844.
- 32 X. Chen, D. Zhou, W. Xu, J. Zhu, G. Pan, Z. Yin, H. Wang, Y. Zhu, C. Shaobo and H. Song, *Scientific Reports 2017 7:1*, 2017, **7**, 1–8.
- 33 J. He, W. Zheng, F. Ligmajer, C. F. Chan, Z. Bao, K. L. Wong, X. Chen, J. Hao, J. Dai, S. F. Yu and D. Y. Lei, *Light: Science & Applications* 2017 6:5, 2016, **6**, e16217–e16217.

- 34 W. Ye, Q. Huang, X. Jiao, X. Liu and G. Hu, *J Alloys Compd*, 2017, **719**, 159–170.
- 35 H. Liu, J. Xu, H. Wang, Y. Liu, Q. Ruan, Y. Wu, X. Liu, J. K. W Yang, H. Liu, H. Wang, Y. Liu, Q. Ruan, J. K. W Yang, J. Xu, Y. Wu and X. Liu, *Advanced Materials*, 2019, **31**, 1807900.
- 36 M. Saboktakin, X. Ye, S. J. Oh, S. H. Hong, A. T. Fafarman, U. K. Chettiar, N. Engheta, C. B. Murray and C. R. Kagan, *ACS Nano*, 2012, **6**, 8758–8766.
- 37 H. Qian, Z. Li and Y. Zhang, *Nanotechnology*, 2008, **19**, 345606.
- 38 A. Das, C. Corbella Bagot, E. Rappeport, T. Ba Tis and W. Park, *J Appl Phys*, 2021, **130**, 23102.
- 39 X. Ye, J. E. Collins, Y. Kang, J. Chen, D. T. N. Chen, A. G. Yodh and C. B. Murray, *Proc Natl Acad Sci U S A*, 2010, **107**, 22430–22435.
- 40 X. Liu, Y. Ni, C. Zhu, L. Fang, J. Kou, C. Lu and Z. Xu, *Nanotechnology*, 2016, **27**, 295605.
- 41 Y. Ren, M. Chen, L. Hu, X. Fang and L. Wu, *Journal of Materials Chemistry*, 2012, **22**, 944-950
- 42 F. Reincke, W. K. Kegel, H. Zhang, M. Nolte, D. Wang, D. Vanmaekelbergh and H. Möhwald, *Physical Chemistry Chemical Physics*, 2006, **8**, 3828–3835.
- 43 A. L. Thangawng, R. S. Ruoff, M. A. Swartz and M. R. Glucksberg, *Biomed Microdevices*, 2007, **9**, 587–595.
- 44 I. Byun and J. Kim, *Journal of Micromechanics and Microengineering*, 2010, **20**, 055024.
- 45 H. J. Levinson, *Principles of Lithography*, SPIE, 4th Editio., 2019.
- 46 J. Pu, Y. Yomogida, K. K. Liu, L. J. Li, Y. Iwasa and T. Takenobu, *Nano Lett*, 2012, **12**, 4013–4017.
- 47 B. Ruben, M. Elisa, L. Leandro, M. Victor, G. Gloria, S. Marina, S. K. Mian, R. Pandiyan and L. Nadhira, *Micro Nano Lett*, 2017, **12**, 754–757
- 48 C. Y. Li and Y. C. Liao, ACS Appl Mater Interfaces, 2016, **8**, 11868–11874.